



Article

Dynamic Analysis and Field-Programmable Gate Array Implementation of a 5D Fractional-Order Memristive Hyperchaotic System with Multiple Coexisting Attractors

Fei Yu ^{1,*} , Wuxiong Zhang ¹, Xiaoli Xiao ¹, Wei Yao ¹, Shuo Cai ¹, Jin Zhang ¹ , Chunhua Wang ² and Yi Li ³

¹ School of Computer and Communication Engineering, Changsha University of Science and Technology, Changsha 410114, China; zhangwuxiong2333@163.com (W.Z.); xxl@csust.edu.cn (X.X.); yaowei@csust.edu.cn (W.Y.); caishuo@csust.edu.cn (S.C.); mail_zhangjin@163.com (J.Z.)

² College of Computer Science and Electronic Engineering, Hunan University, Changsha 410082, China; wch1227164@hnu.edu.cn

³ Hunan Post & Telecommunication Planning and Designing Institute, No. 236 Yuanda Road, Changsha 410126, China; 15308406988@189.cn

* Correspondence: yufeiyfyf@csust.edu.cn

Abstract: On the basis of the chaotic system proposed by Wang et al. in 2023, this paper constructs a 5D fractional-order memristive hyperchaotic system (FOMHS) with multiple coexisting attractors through coupling of magnetic control memristors and dimension expansion. Firstly, the divergence, Kaplan–Yorke dimension, and equilibrium stability of the chaotic model are studied. Subsequently, we explore the construction of the 5D FOMHS, introducing the definitions of the Caputo differential operator and the Riemann–Liouville integral operator and employing the Adomian resolving approach to decompose the linears, the nonlinears, and the constants of the system. The complex dynamic characteristics of the system are analyzed by phase diagrams, Lyapunov exponent spectra, time-domain diagrams, etc. Finally, the hardware circuit of the proposed 5D FOMHS is performed by FPGA, and its randomness is verified using the NIST tool.

Keywords: memristor; fractional-order memristive hyperchaotic system; coexisting attractors; FPGA

MSC: 37D45; 34C28; 37N30; 65P20



Citation: Yu, F.; Zhang, W.; Xiao, X.; Yao, W.; Cai, S.; Zhang, J.; Wang, C.; Li, Y. Dynamic Analysis and Field-Programmable Gate Array Implementation of a 5D Fractional-Order Memristive Hyperchaotic System with Multiple Coexisting Attractors. *Fractal Fract.* **2024**, *8*, 271. <https://doi.org/10.3390/fractalfract8050271>

Academic Editors: António Lopes and Yangquan Chen

Received: 25 February 2024

Revised: 12 April 2024

Accepted: 28 April 2024

Published: 1 May 2024



Copyright: © 2024 by the authors. Licensee MDPI, Basel, Switzerland. This article is an open access article distributed under the terms and conditions of the Creative Commons Attribution (CC BY) license (<https://creativecommons.org/licenses/by/4.0/>).

1. Introduction

Chaos, also known as nonlinear dynamics, is characterized by its significant sensitivity to initial conditions in deterministic systems, quasi-random attributes, and unique, non-repeating trajectories. Nonlinear science is theoretically significant and promising for practical applications across various life aspects. Over the past decade, researchers have extensively applied it in fields such as image encryption [1–5], electronic circuits [6–10], chaos synchronization [11–15], pseudo-random number generators [16–20], and neural networks [21–25], among others. The complex structure of chaotic attractors enhances their dynamic properties. Researchers have introduced a variety of chaotic systems with intricate dynamic behaviors, incorporating unique nonlinear terms, extending dimensionality, and constructing functions. These include hyperchaotic attractors [26–30], hidden attractors [31–35], conservative chaotic attractors [36–39], and multi-wing and multi-scroll attractors [40–43]. High-dimensional chaotic systems offer a more complex structure, intricate dynamic behavior, and greater randomness than low-dimensional ones, making hyperchaotic systems increasingly interesting to researchers. The main characteristic of hyperchaotic systems is that they have two or more Lyapunov exponents, which enhances their security relative to traditional chaotic systems. System structures have evolved iteratively, showing greater application potential. For example, a new 2D hyperchaotic system based on Schaffer mapping is introduced in [44], exhibiting optimal ergodic and uncertain

characteristics. Al proposed a hyperchaotic system without equilibrium points in [45], characterized by high Lyapunov exponents and complex dynamical behaviors. Based on the 5D Euler equation, Huang et al. [46] proposed a 5D non-equilibrium Hamiltonian conservative chaotic system with multiple coexisting attractors and hyperchaotic attractors.

The memristor is an electronic device whose resistance varies with the direction and magnitude of current flow. It possesses characteristics such as nanometer-scale size, automatic memory, low power consumption, and nonlinearity, making it highly suitable as a nonlinear component in chaotic circuits. Compared to traditional chaotic circuits, memristor-based chaotic circuits are extremely sensitive to circuit parameters, with subtle differences in memristor initial values having significant impacts. Additionally, chaotic circuits can generate numerous intriguing and more complex chaotic phenomena. Based on this, researchers have proposed various complex chaotic systems based on memristors. Kong et al. introduced a new memristor model in [47]. Then, the authors constructed a 6D fractional-order memristive Hopfield neural network system based on the memristor model, which has multiple steady-state characteristics and good randomness. Sun et al. [48] applied memristors to Pavlov associative memory, achieving multiple generalization and differentiation processes. Yu et al. [49] designed a novel locally active non-volatile memristor and constructed a 4D memristive Hopfield neural network by introducing this memristor. Yao et al. developed a new memristor model in [50] and constructed an asymmetric memristive Hopfield neural network using this memristor model.

In the latter half of the twentieth century, fractional calculus emerged as an abstract mathematical theory. Fractional calculus is an extension of traditional calculus to arbitrary real or complex orders of differentiation and integration. Compared to integer-order calculus, fractional calculus provides a more accurate description of memory effects and historical dependencies in many complex systems, making it more aligned with the real world. In recent years, scientists from various fields and backgrounds have been studying this theory and its applications from different perspectives, including nonlinear dynamics. Scientists can use fractional calculus to model and analyze the dynamics of systems related to anomalous phenomena. Therefore, fractional calculus theory can be applied to chaotic systems. Initially, by introducing fractional differentiation operators to integer-order chaotic systems, the system remains chaotic with rich dynamic characteristics and potential applications. More and more researchers have joined the study, proposing chaotic systems with fractional operators exhibiting diverse characteristics. Matouk [51] conducted reasoning and inference based on gamma functions and left-right Caputo fractional differentiation operators, deriving some secondary properties. They constructed a new fractional parameter with higher degrees of freedom compared to ordinary operators, exhibiting more complex dynamic behavioral characteristics. Lei et al. [52] established a new fractional-order model based on Hindmarsh Rose neurons in an electric field environment. Through the Adomian resolving approach, they decomposed each nonlinear term and analyzed the firing behavior of the neuron model. Zeng [53] applied fractional calculus to a fractional-order infectious disease model, and the authors used the Laplace Adomian solution method to effectively obtain approximate solutions with fewer iterations.

This paper proposes a 5D fractional-order memristive hyperchaotic system (FOMHS) with only three nonlinear terms and investigates its nonlinear dynamic behavior. The system exhibits complex dynamic behavior, including extreme multistability phenomena such as the coexistence of periodic and chaotic states. Secondly, we use the Adomian decomposition method to decompose the nonlinear, linear, and constant terms of the system, in order to provide a more comprehensive observation of its physical structure. Finally, we implemented 5D FOMHS on FPGA hardware to verify its functionality. In addition, we also tested the components of the system against NIST standards, demonstrating its potential for secure communication.

The remaining work is scheduled as follows: In Section 2, we compute the equilibrium points and analyze the divergence of the integer-order system, demonstrating its properties characteristic of hyperchaotic systems. In Section 3, we utilize the Adomian resolving

approach to obtain various numerical solutions for the 5D FOMHS system and investigate its dynamic characteristics through diverse simulations. Subsequently, in Section 4, we design and implement the digital circuit for the 5D FOMHS. In Section 5, we assess the randomness of sequences generated by the system using the NIST suite and visualize the results with histograms and tables. Finally, we summarize the research findings of the entire project and discuss potential areas for future investigation in Section 6.

2. A 5D Integer-Order Memristive Hyperchaotic System

Recently, Wang et al. [54] proposed a simple hyperchaotic system. This paper transforms it into a 5D hyperchaotic system. The mathematical model is as follows:

$$\begin{cases} \dot{x} = a(w - x), \\ \dot{y} = -w, \\ \dot{z} = xw - bz, \\ \dot{w} = -xz + cw + dy, \\ \dot{u} = -w + kx(m + 3nu^2), \end{cases} \quad (1)$$

where x, y, z, w, u are system state variables and a, b, c, k, m, n are coupling parameters. $W(u)$ is the memristor, and the memristor function is $w(u) = e + 3nu^2$. The system (1) exhibits rich dynamic characteristics as self-excited chaotic attractors, and the shape and extent of attractors are influenced by initial conditions (ICs), periods, and control parameters. The system (1) divergence is:

$$\nabla V = \frac{\partial \dot{x}}{\partial x} + \frac{\partial \dot{y}}{\partial y} + \frac{\partial \dot{z}}{\partial z} + \frac{\partial \dot{w}}{\partial w} + \frac{\partial \dot{u}}{\partial u} = -a - b + c + 6nkxu. \quad (2)$$

when $-a - b + c + 6nkxu = 1$, the system (1) is a conservative chaotic system; when $-a - b + c + 6nkxu < 1$, the system (1) is a dissipative chaotic system.

Take $a = 20, b = 2, c = 10, d = 4, k = 10, m = 0.1, n = 0.01$, and set the IC to $[1, 1, 2, 1, 1]$. When the calculation time is 1000 seconds and the iteration step is 0.01, the Lyapunov exponent spectrum of the system (1) is shown in Figure 1. The final Lyapunov exponents are:

$$\begin{cases} LE_1 = 0.312401 \\ LE_2 = 0.117056 \\ LE_3 = -0.006177 \\ LE_4 = -0.415351 \\ LE_5 = -11.822570 \end{cases} \quad \sum_{i=1}^5 LE_i \approx -12.5741. \quad (3)$$

The Kaplan–York dimension provides a method for quantifying the self similarity of chaotic systems. It is obtained by correlating and calculating the trajectory of the system in phase space. Given the aforementioned conditions for Lyapunov exponents, The Kaplan–York dimension of system (1) can be calculated as follows:

$$\begin{aligned} D_{LE} &= j + \frac{1}{|LE_{j+1}|} \sum_{i=1}^j LE_i, \\ D_{LE} &= 4 + \frac{LE_1 + LE_2 + LE_3 + LE_4}{|LE_5|} \approx 4.00067. \end{aligned} \quad (4)$$

From Figure 1, it can be seen that there are two positive Lyapunov exponents, indicating the existence of hyperchaotic phenomena in system (1). Furthermore, the calculated Kaplan–Yorke dimension exceeds 4, which is the dimensionality of the system as indicated by the result in the Kaplan–Yorke dimension formula. This result substantiates the system's chaotic state under these conditions.

Phase diagrams can describe complex dynamic behaviors, including periodic orbits and chaotic attractors. The phase diagrams of (1) are shown in Figure 2a–d. The time series of x is depicted in Figure 2e.

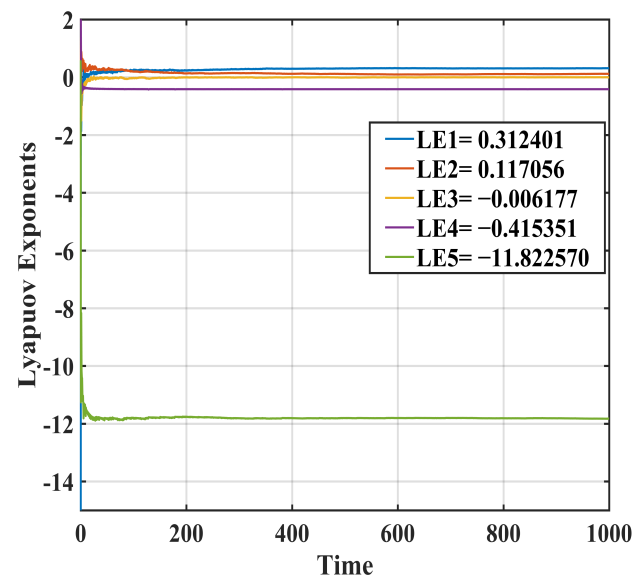


Figure 1. Lyapunov exponent spectrum of system (1).

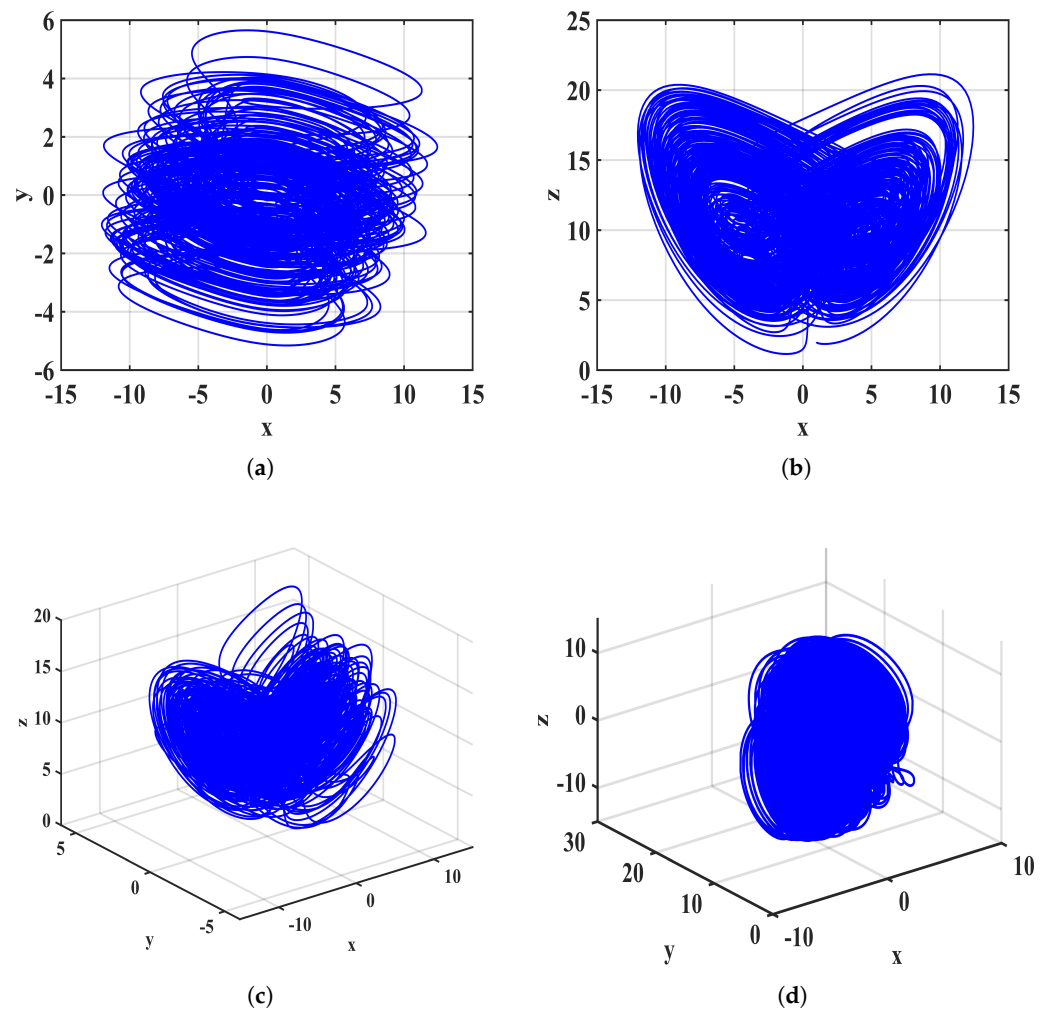


Figure 2. Cont.

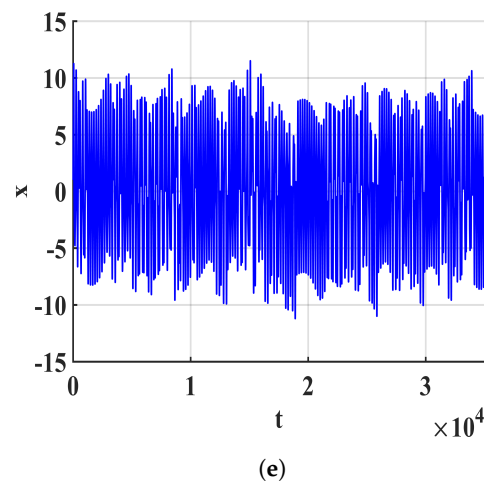


Figure 2. Phase diagrams and time series of the system (1). (a) $x - y$ plane, (b) $x - z$ plane, (c) $x - y - z$ space, (d) $y - z - w$ space, (e) time series of x .

2.1. Equilibrium Stability Analysis

For the system (1), when $\dot{x} = \dot{y} = \dot{z} = \dot{w} = \dot{u} = 0$, the equilibrium points can be expressed as:

$$E = (x^* = 0, y^* = 0, z^* = 0, w^* = 0, u^* = 0). \quad (5)$$

The Jacobian matrix of the response is:

$$J = \begin{pmatrix} -a & 0 & 0 & a & 0 \\ 0 & 0 & 0 & -1 & 0 \\ w & -b & 0 & x & 0 \\ -z & d & -x & c & 0 \\ k(m + 3nuu) & 0 & 0 & -1 & 6knxu \end{pmatrix}. \quad (6)$$

Substitute the conclusion of Equation (5) into Equation (6), and we can obtain:

$$J = \begin{pmatrix} -a & 0 & 0 & a & 0 \\ 0 & 0 & 0 & -1 & 0 \\ 0 & 0 & -b & 0 & 0 \\ 0 & d & 0 & c & 0 \\ km & 0 & 0 & -1 & 0 \end{pmatrix}. \quad (7)$$

J has the characteristic equation:

$$(-\lambda)(-\lambda - a)(-\lambda - b)(\lambda^2 - c\lambda + d) = 0, \quad (8)$$

the final root is:

$$\begin{cases} \lambda_1 = 0, \\ \lambda_2 = -a, \\ \lambda_3 = -b, \\ \lambda_4 = \frac{c + \sqrt{c^2 - 4d}}{2}, \\ \lambda_5 = \frac{c - \sqrt{c^2 - 4d}}{2}. \end{cases} \quad (9)$$

If all eigenvalues of an equilibrium point have negative real parts, then the equilibrium point is stable. On the contrary, if at least one eigenvalue contains a positive real part, then the equilibrium point is unstable. For example, setting the parameters to $a = 20$, $b = 2$, $c = 10$, $d = 4$, $k = 10$, $m = 0.1$, and $n = 0.01$ results in the system exhibiting a hyperchaotic state with eigenvalues $\lambda_1 = 0$, $\lambda_2 = -20$, $\lambda_3 = -2$, $\lambda_4 = 5 + \sqrt{21}$, and $\lambda_5 = 5 - \sqrt{21}$,

indicating two positive eigenvalues. Hence, the equilibrium point is a saddle node of index 2.

2.2. Nonlinear Dynamic Behavior Analysis

When the parameters are fixed at $a = 25$, $c = 10$, $d = 4$, $k = 10$, $m = 0.1$, $n = 0.01$, and the initial conditions (ICs) are set to $[1, 1, 1, 1, 1]$, the control parameter b is varied within the interval $[0.6, 1.5]$. Simulations are conducted using Matlab2017a over an iteration time of 3000 s. To more clearly observe changes in the system state, after disregarding the negligible Lyapunov exponents in the fifth dimension, the Lyapunov exponent spectrum is displayed in Figure 3a. The bifurcation diagram is shown in Figure 3b. The exponent spectrum reveals that the system exhibits a rich array of dynamic behavior changes. Although a positive Lyapunov exponent appears in Figure 3a when $b = 0.6$, in the context of chaotic systems, a Lyapunov exponent with an absolute value closest to zero is conventionally considered as zero. Thus, for $b \in [0.6, 0.81)$, the system (1) displays no positive Lyapunov exponents and remains in a periodic state. The bifurcation diagram in Figure 3b indicates that for $b \in [0.7, 0.77]$, the system (1) undergoes periodic doubling bifurcation before returning to a periodic state. For $b \in [0.81, 0.88)$, the system exhibits a positive Lyapunov exponent, as shown in Figure 3a, and the bifurcation diagram in Figure 2b indicates that the system transitions into a chaotic state. At $b = 0.88$, the system reenters a periodic state; for $b \in (0.87, 1)$, it transitions back to chaos; and for $b \in (1, 1.5)$, the exponent spectrum in Figure 3a shows two positive values for the first time, marking the system's entry into a hyperchaotic state through iteration.

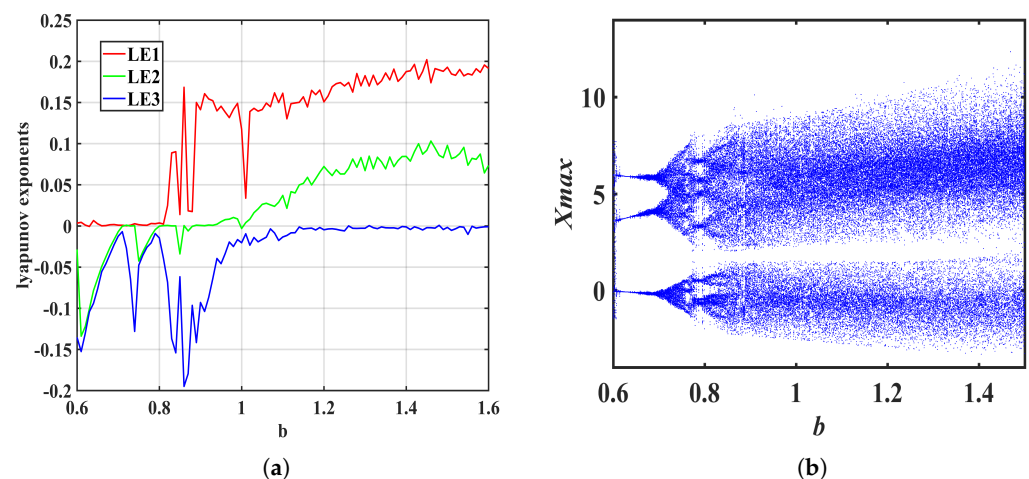


Figure 3. Lyapunov exponent spectrum and phase diagram of the system (1). (a) Lyapunov exponent spectrum, (b) bifurcation diagram.

2.3. Coexisting of Attractors

In chaotic systems, an attractor is a state in which the system tends to stabilize after a long period of evolution. Coexisting attractors are a complex dynamic property of chaotic systems. This indicates that dissipative systems with the same control parameters but different ICs can exhibit partially overlapping trajectories and potentially different stable states.

For the system (1), with parameters set as $a = 20$, $c = 11$, $d = 3$, $m = 0.1$, $n = 0.01$, and $k = 6$, two states are defined: State 1 with $y_1 = [1, 1, 1, 1, 1]$ is represented in blue, and State 2 with $y_2 = [-1, -1, -1, -1, -1]$ is represented in red. When $b = 6$, 2D phase diagrams present a symmetrical state, and the 3D phase diagrams do not interfere with each other. States 1 and 2 exhibit chaotic coexistence. The phase diagrams on the $x - w$ plane and the $x - y - z$ space are shown in Figures 3b and 4a, respectively. When the parameter b is adjusted to 13, the phase diagrams show periodic cycles and do not interfere with each other. States 1 and 2 transition to periodic coexistence, represented by green and

black colors, respectively. The corresponding phase diagrams on the $x - w$ plane and the $x - y - z$ space are presented in Figure 4c,d.

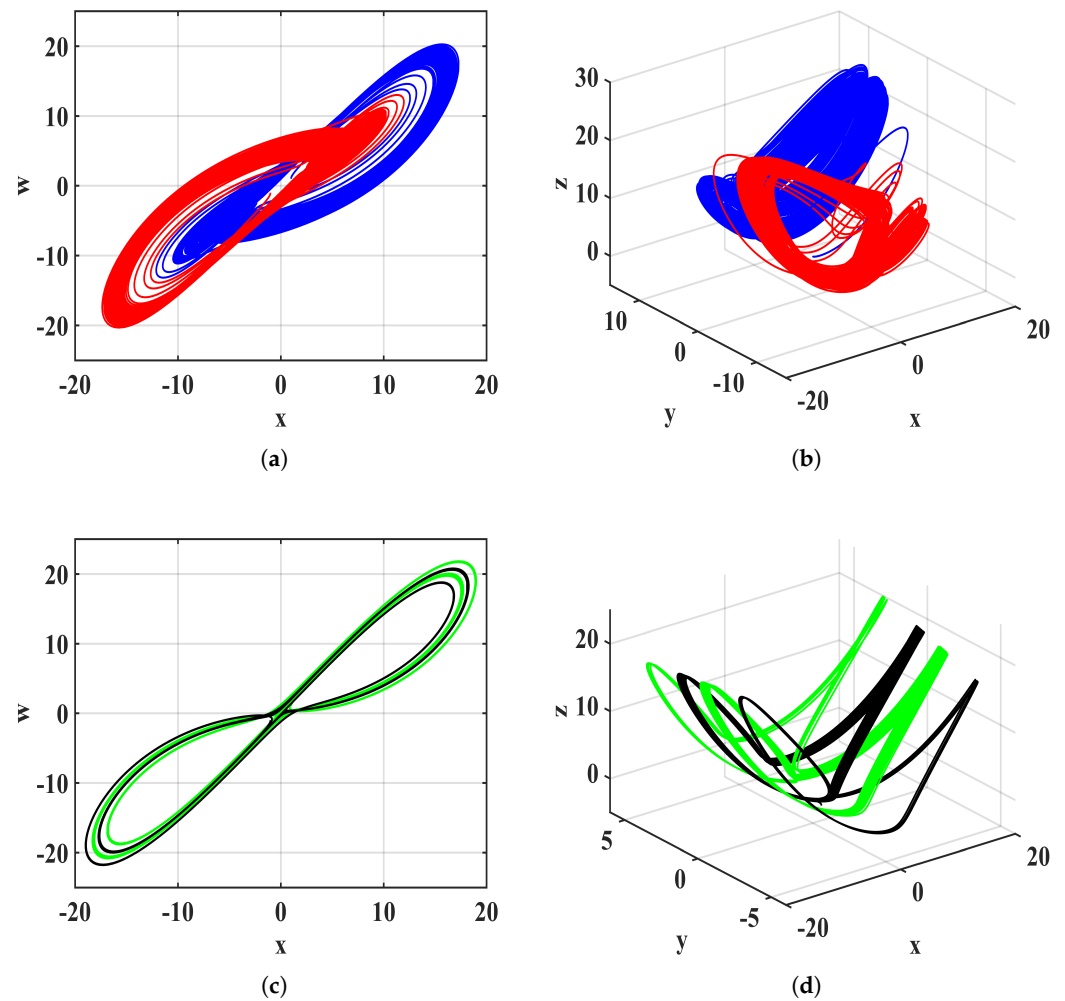


Figure 4. The coexisting phase diagrams of State 1 and State 2. (a) Chaotic coexistence on the $x - w$ plane, (b) chaotic coexistence on the $x - y - z$ space, (c) periodic coexistence on the $x - w$ plane, (d) periodic coexistence on the $x - y - z$ space.

3. 5D FOMHS

3.1. System Decomposition

In Ref. [55], the definition of Caputo differentiation is determined by Equation (10).

$${}^*D_{t_0}^q x(t) = J_{t_0}^{m-q} D_{t_0}^m x(t) = \begin{cases} \frac{1}{\Gamma(m-q)} \int_{t_0}^t (t-\tau)^{(m-q-1)} x^{(m)}(\tau) d\tau, & m-1 < q < m, \\ \frac{d^m}{dt^m} x(t), & q = m, \end{cases} \quad (10)$$

$\Gamma(\cdot)$ is the gamma function. ${}^*D_{t_0}^q$ is Caputo differential operator, its order is q , $q \in \mathbb{R}^+$, $m \in \mathbb{N}$.

The Riemann–Liouville fractional integral can be defined as:

$$J_{t_0}^q x(t) = \int_{t_0}^t (t-\tau)^{(q-1)} x(\tau) d\tau, \quad (11)$$

$J_{t_0}^q x(t)$ is an integral operator of q order, $q \in R^+, t \in [t_0, t_1]$. When $m - 1 < q < m$, the Caputo differentiation and Riemann–Liouville fractional integration will have some special properties, such as:

$$*D_{t_0}^q x(t) = J_{t_0}^q x(t) = x(t), \tag{12}$$

$$J_{t_0}^q (*D_{t_0}^q)x(t) = x(t) - \sum_{k=0}^{m-1} x^{(k)}(t_0^+) \frac{(t - t_0)^k}{k!}. \tag{13}$$

Based on the above definition and special properties, for fractional-order systems:

$$*D_{t_0}^q x(t) = f(x(t) + g(t)), \tag{14}$$

$x(t) = [x_1(t), x_2(t), x_3(t), \dots, x_n(t)]^T$ represents the given function variable in compound function f ; $g(t) = [g_1(t), g_2(t), g_3(t), \dots, g_n(t)]^T$ represents a constant. Finally, the fractional-order system can be decomposed into three parts using the Adomian resolving approach:

$$\begin{aligned} *D_{t_0}^q x(t) &= Lx(t) + Nx(t) + g(t), \\ x^{(k)}(t_0)^+ &= b_k, k = 0, \dots, m - 1, \\ m \in N, m - 1 < q \leq m, \end{aligned} \tag{15}$$

$Lx(t)$ is a linear term of the fractional-order system, and $Nx(t)$ is a nonlinear term of the fractional-order system. The ICs integrate with Equation (15) and bring it into the ICs and finally decompose the nonlinear term into:

$$A_j^i = \frac{1}{i!} \left[\frac{d^i}{d\lambda^i} N(v_j^i(\lambda)) \right]_{\lambda=0} v_j^i(\lambda) = \sum_{k=0}^i (\lambda)^k x_j^k. \tag{16}$$

The non-linear term is written as:

$$Nx = \sum_{i=0}^{\infty} A^i(x^0, x^1, \dots, x^i), \tag{17}$$

since the solution of the equation is $x = \sum_{i=0}^{\infty} x^i$ based on Equation (16), the solution of the equation can be written as:

$$\begin{cases} x^0 = J_{t_0}^q g + \sum_{k=0}^{m-1} b_k \frac{(t-t_0)^k}{k!}, \\ x^1 = J_{t_0}^q Lx_0 + J_{t_0}^q A^0(x^0), \\ x^2 = J_{t_0}^q Lx_1 + J_{t_0}^q A^1(x^0, x^1), \\ x^3 = J_{t_0}^q Lx_2 + J_{t_0}^q A^2(x^0, x^1, x^2), \\ \vdots \\ x^i = J_{t_0}^q Lx_{i-1} + J_{t_0}^q A^{i-1}(x^0, x^1, \dots, x^{i-1}). \end{cases} \tag{18}$$

So as to increase the flexibility and complexity of the system, a fractional-order is introduced to the system (1):

$$\begin{cases} *D_{t_0}^q x = a(w - x), \\ *D_{t_0}^q y = -w, \\ *D_{t_0}^q z = xw - bz, \\ *D_{t_0}^q w = -xz + cw + dy, \\ *D_{t_0}^q u = -w + kx(m + 3nu^2), \end{cases} \tag{19}$$

where q is a fractional-order, and the ICs are:

$$\begin{cases} x^0 = x(t_0) = c_1^0, \\ y^0 = y(t_0) = c_2^0, \\ z^0 = z(t_0) = c_3^0, \\ w^0 = w(t_0) = c_4^0, \\ u^0 = u(t_0) = c_5^0. \end{cases} \quad (20)$$

According to Equations (19) and (20) and the properties of fractional integral, we can obtain:

$$\begin{cases} x_1^1 = (a(c_4^0 - c_1^0)) \frac{t-t_0^q}{\Gamma(q+1)}, \\ y_2^1 = (-c_4^0) \frac{t-t_0^q}{\Gamma(q+1)}, \\ z_3^1 = (c_1^0 c_4^0 - bc_3^0) \frac{t-t_0^q}{\Gamma(q+1)}, \\ w_4^1 = (-c_1^0 + cc_4^0 + dc_2^0) \frac{t-t_0^q}{\Gamma(q+1)}, \\ u_5^1 = (-c_4^0 + kc_1^0(m + 3nc_5^0 c_5^0)) \frac{t-t_0^q}{\Gamma(q+1)}. \end{cases} \quad (21)$$

Variables are assigned to corresponding coefficients:

$$\begin{cases} c_1^1 = a(c_4^0 - c_1^0), \\ c_2^1 = -c_4^0, \\ c_3^1 = c_1^0 c_4^0 - bc_3^0, \\ c_4^1 = -c_1^0 + cc_4^0 + dc_2^0, \\ c_5^1 = -c_4^0 + kc_1^0(m + 3nc_5^0 c_5^0). \end{cases} \quad (22)$$

So, $x_1 = c_1 \frac{t-t_0^q}{\Gamma(q+1)}$. Based on this, we calculate the coefficients of other terms:

$$\begin{cases} c_1^2 = a(c_4^1 - c_1^1), \\ c_2^2 = -c_4^1, \\ c_3^2 = c_1^1 c_4^1 - bc_3^1 + c_1^0 c_4^1, \\ c_4^2 = -c_1^1 c_3^1 - c_1^0 c_3^1 + cc_4^1 + dc_2^1, \\ c_5^2 = -c_4^1 + kmc_1^1 + 3nk c_5^0 (c_1^1 c_5^1 + c_1^0 c_5^1) \frac{\Gamma(2q+1)}{\Gamma(q+1)}, \end{cases} \quad (23)$$

and

$$\begin{cases} c_1^3 = a(c_4^2 - c_1^2), \\ c_2^3 = -c_4^2, \\ c_3^3 = c_1^2 c_4^2 + c_1^1 c_4^2 \frac{\Gamma(2q+1)}{\Gamma(q+1)} + c_1^0 c_4^2 - bc_3^2, \\ c_4^3 = -c_1^2 c_3^2 - c_1^1 c_3^2 \frac{\Gamma(2q+1)}{\Gamma(q+1)} - c_1^0 c_3^2 + cc_4^2 + dc_2^2, \\ c_5^3 = -c_4^2 + kmc_1^2 + 3nk [c_5^1 c_5^1 (c_1^2 + c_1^1 \frac{\Gamma(2q+1)}{\Gamma(q+1)}) + c_5^0 c_5^1 (c_1^2 + c_1^1 \frac{\Gamma(2q+1)}{\Gamma(q+1)})]. \end{cases} \quad (24)$$

Finally, the system solution is obtained:

$$\begin{cases} x(t) = c_1^0 + c_1^1 \frac{t-t_0^q}{\Gamma(q+1)} + c_2^1 \frac{t-t_0^{2q}}{\Gamma(2q+1)} + c_3^1 \frac{t-t_0^{3q}}{\Gamma(3q+1)}, \\ y(t) = c_2^0 + c_2^1 \frac{t-t_0^q}{\Gamma(q+1)} + c_2^2 \frac{t-t_0^{2q}}{\Gamma(2q+1)} + c_2^3 \frac{t-t_0^{3q}}{\Gamma(3q+1)}, \\ z(t) = c_3^0 + c_3^1 \frac{t-t_0^q}{\Gamma(q+1)} + c_3^2 \frac{t-t_0^{2q}}{\Gamma(2q+1)} + c_3^3 \frac{t-t_0^{3q}}{\Gamma(3q+1)}, \\ w(t) = c_4^0 + c_4^1 \frac{t-t_0^q}{\Gamma(q+1)} + c_4^2 \frac{t-t_0^{2q}}{\Gamma(2q+1)} + c_4^3 \frac{t-t_0^{3q}}{\Gamma(3q+1)}, \\ u(t) = c_5^0 + c_5^1 \frac{t-t_0^q}{\Gamma(q+1)} + c_5^2 \frac{t-t_0^{2q}}{\Gamma(2q+1)} + c_5^3 \frac{t-t_0^{3q}}{\Gamma(3q+1)}. \end{cases} \quad (25)$$

The parameters are set to $a = 25$, $b = 2$, $c = 10$, $d = 4$, $k = 10$, $m = 0.1$, and $n = 0.01$. With the IC = $[1, 1, 2, 1, 1]$, the order set at 0.7, and the number of iterations set at 10,000, the 2D phase diagrams on the $x - y$ and $x - z$ planes are presented in Figures 5a and 5b, respectively. Additionally, the 3D phase diagrams on the $x - y - z$ space and $y - z - w$ space are illustrated in Figure 5c,d. The final time series diagram of x is depicted in Figure 5e.

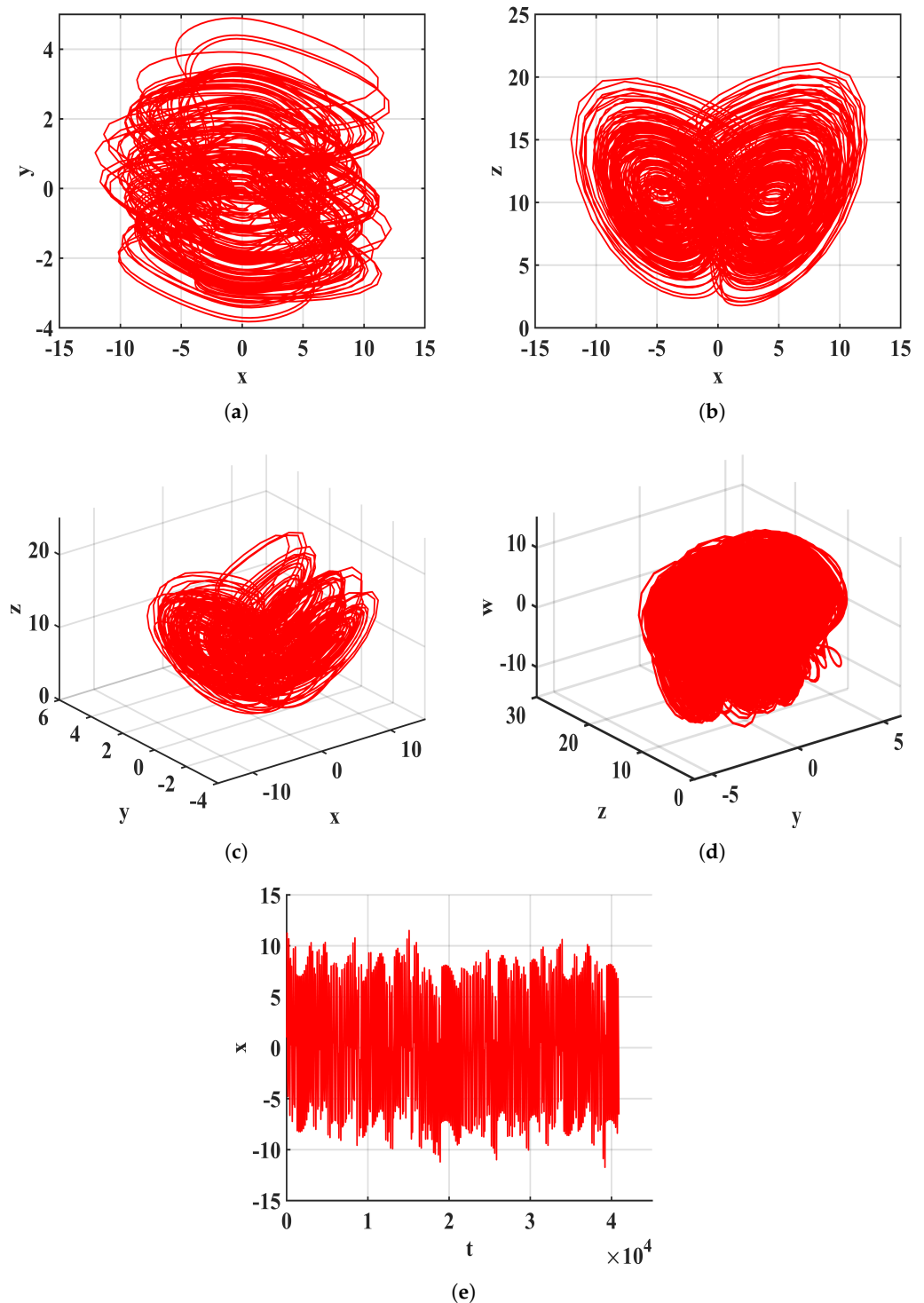


Figure 5. Phase diagrams and time series of the system (19). (a) $x - y$ plane, (b) $x - z$ plane, (c) $x - y - z$ space, (d) $y - z - w$ space, (e) time series of x .

3.2. Dynamic Analysis of the 5D FOMHS

The Lyapunov exponent spectrum, consisting of three lines, represents the system's characteristics and is calculated with the ICs set to $[1, 1, 1, 1, 1]$. The parameters are as follows: $b = 2$, $c = 7$, $d = 4$, $k = 5$, $m = 0.1$, $n = 0.01$. The fractional-order system, denoted as (19), is characterized by an order of $e = 0.7$, with 20,000 iterations and a step size of 0.005, operating within the parameter range of $[10, 14]$. The Lyapunov exponent spectrum, depicted in Figure 6a, shows that when a varies within the interval $[10, 11]$, the three lines consistently remain close to or below zero, indicating no positive Lyapunov exponents and positioning the system (19) in a periodic state. When a lies within $[12.5, 12.8]$ or $[13.2, 13.4]$, a positive Lyapunov exponent emerges, signaling a chaotic state for the fractional-order system. When d is within $[13.5, 14]$, the green line stays closer to zero compared to the blue and red lines, resulting in two positive Lyapunov exponents and suggesting that the system consistently exhibits hyperchaotic behavior within this interval. This demonstrates that the fractional-order system retains the hyperchaotic characteristics of its integer-order counterpart while still exhibiting complex dynamic changes. The dense clustering of points in the bifurcation diagram, shown in Figure 6b, further illustrates this phenomenon.

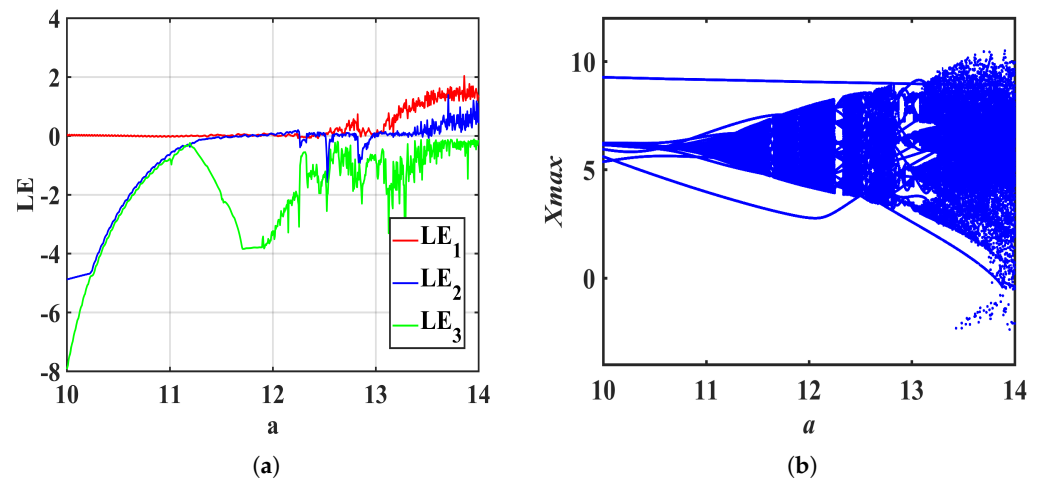


Figure 6. Lyapunov exponent spectrum and bifurcation diagram of system (19) with a in $[10, 14]$. (a) Lyapunov exponent spectrum, (b) bifurcation diagram.

The IC remains unchanged, with the system parameters for the system (19) set as follows: $a = 15$, $c = 7$, $d = 4$, $k = 5$, $m = 0.1$, $n = 0.01$, order $e = 0.7$, the number of iterations at 20,000, and the step size at 0.005. As shown in Figure 7a, the Lyapunov exponent spectrum with b ranging from 1 to 4 reveals complex dynamics. For $b \in [3, 3.9]$, all exponent lines are close to or below zero, indicating a periodic state, especially as the red line—despite being above zero—is closer to it than the blue line, thus considered as zero. In the ranges $b \in [1, 1.2]$ and $[1.3, 1.6]$, the system enters a hyperchaotic state with the whole spectrum showing this characteristic. For $b \in [2, 2.7]$, the system is in a chaotic state, characterized by a positive Lyapunov exponent. Figure 7b, the bifurcation diagram, corresponds to the behaviors depicted in Figure 7a, highlighting the system (19)'s complex dynamics.

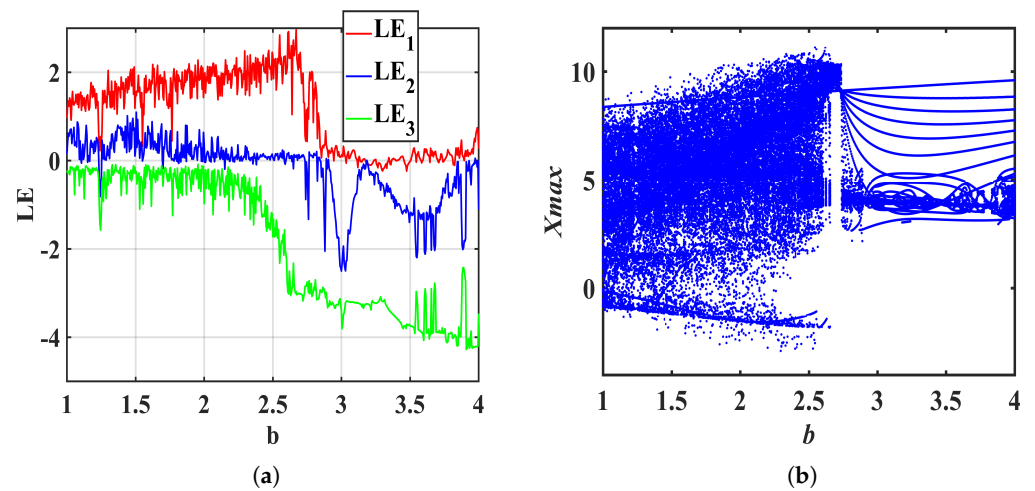


Figure 7. Lyapunov exponent spectrum and bifurcation diagram of the system (19) about b in $[1, 4]$. (a) Lyapunov exponent spectrum, (b) bifurcation diagram.

The IC is still $[1, 1, 1, 1, 1]$, and the system (19) parameter settings are $a = 15$, $b = 2$, $d = 4$, $k = 5$, $m = 0.1$, $n = 0.01$, and order e is 0.7. System (19) parameter c is changed within $[4, 8]$. As can be seen from Figure 8a, when $c \in [4, 4.8]$, the system (19) is in a periodic state; when $c \in [4.8, 7.1]$, the system (19) is in a chaotic state; when $c \in [7.1, 8]$, the system (19) is in a hyperchaotic state. These dynamic behaviors can also be observed by bifurcation of Figure 8b.

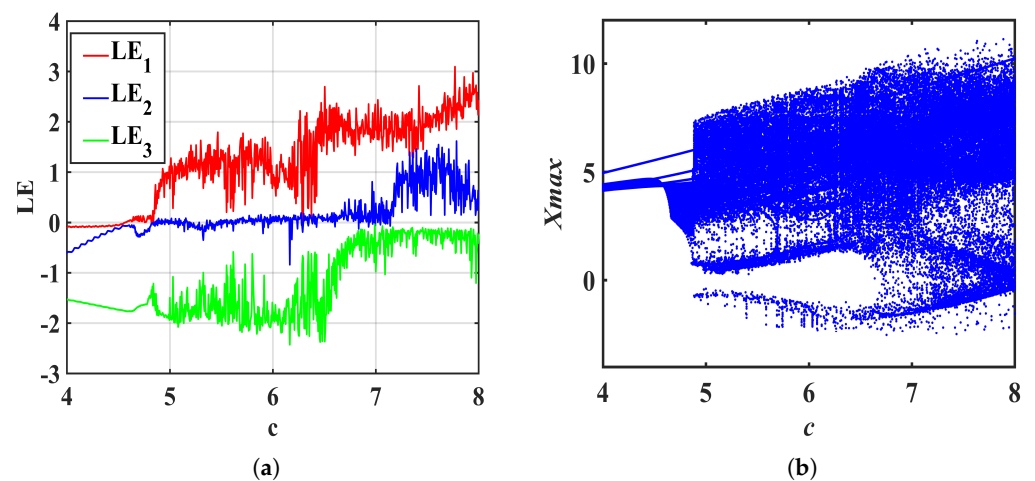


Figure 8. Lyapunov exponent spectrum and bifurcation diagram of the system (19) about c in $[4, 8]$. (a) Lyapunov exponent spectrum, (b) bifurcation diagram.

The IC remains the same, and the parameters are established as follows: $a = 15$, $b = 2$, $c = 6$, $k = 5$, $m = 0.1$, $n = 0.01$, order e is 0.7. Parameter d in the system (19) varies within the range $[3, 6]$. According to the exponential spectrum in Figure 9a, when d is between $[3, 3.2]$, the system (19) is in a hyperchaotic state; when d is within $(3.5, 4.3)$, the system shows a hyperchaotic to a chaotic state; when d is between $[4.5, 6]$, the system is in a periodic state. These dynamic behaviors are also visible in the bifurcation diagram shown in Figure 9b.

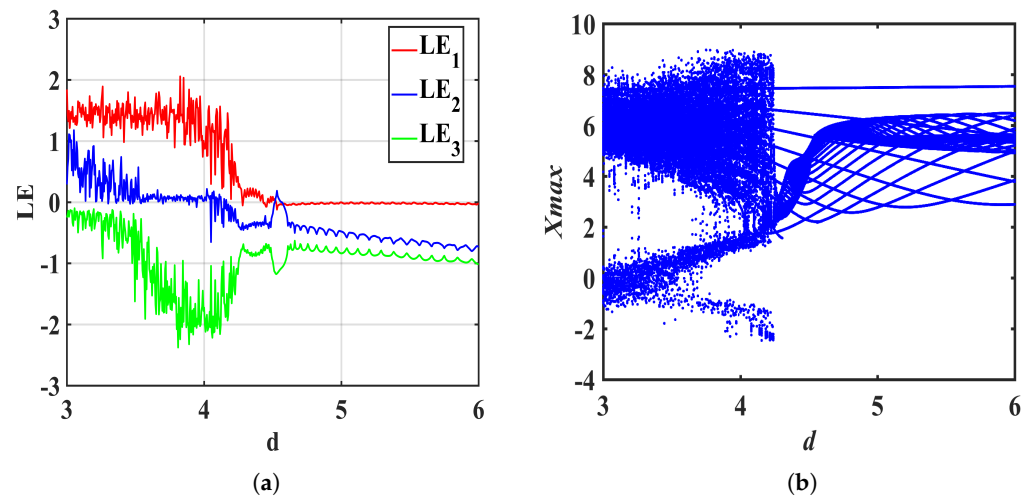


Figure 9. Lyapunov exponent spectrum and bifurcation diagram of the system (19) about d in [3, 6]. (a) Lyapunov exponent spectrum, (b) bifurcation diagram.

3.3. Coexisting of Attractors

Set the order of the fractional-order system to 0.8. The parameters were set: $a = 23.1$, $b = 5$, $c = 10$, $d = 3$, $k = 5$, $m = 0.1$, and $n = 0.01$. Two states were established: State 1, where the IC of the system was set to $[1, 1, 1, 1, 1]$ and represented by the color blue, and State 2, where the IC of the system was $[-1, -1, -1, -1, -1]$ and represented by the color red. Figure 10a,b are the phase diagrams of State 1 and State 2 on the $x-w$ plane and the $x-y-z$ space, respectively. The system (19)'s 2D phase diagram presents a symmetrical state, and the 3D phase diagrams do not interfere with each other. The diagrams depict the chaotic coexistence of States 1 and 2. With all other conditions unchanged and the order set to 0.7, State 3 was introduced with the only change being the color shift from blue to green, maintaining all other conditions identical to State 1. Similarly, State 4 was introduced with the color shifting from red to green, with all other conditions unchanged from State 2. The phase diagrams show periodic cycles and do not interfere with each other. The periodic attractors of State 3 and State 4 were found to coexist. Figure 10c,d are the $x-w$ plane and the $x-y-z$ space, respectively. Compared with integer-order chaotic systems, fractional-order chaotic systems also exhibit the phenomenon of multiple coexisting attractors.

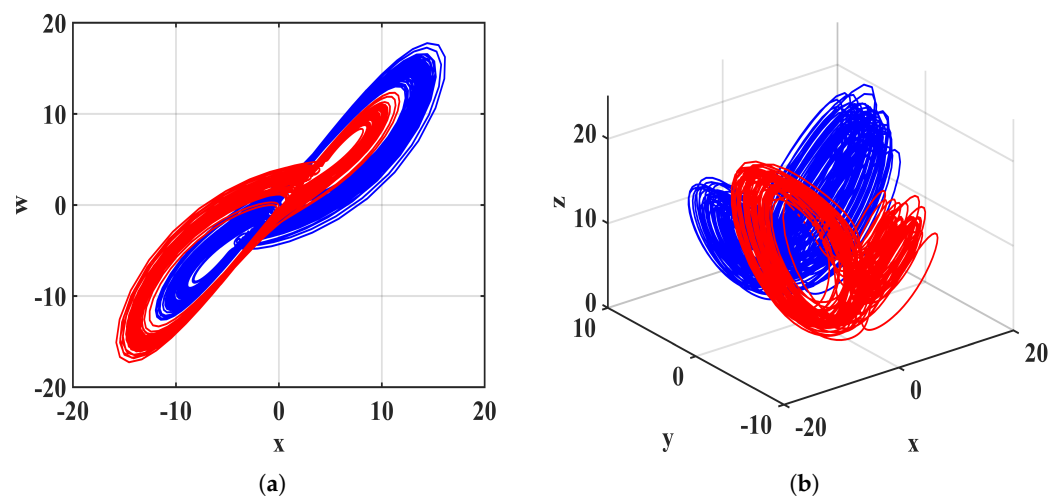


Figure 10. Cont.

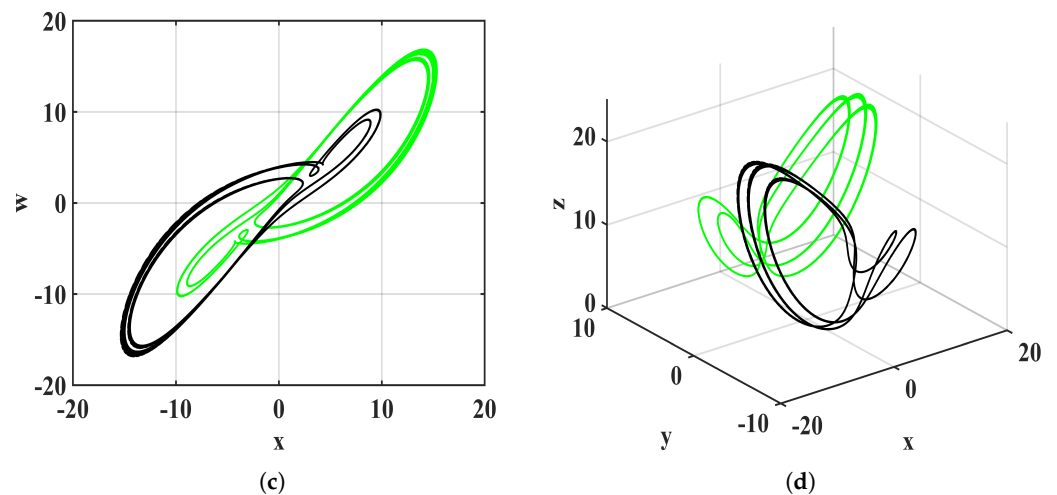


Figure 10. The coexisting phase diagrams of State 1 and State 2 on the $x-w$ plane and the $x-y-z$ plane. (a) Chaotic coexistence on the $x-w$ plane, (b) chaotic coexistence on the $x-y-z$ space, (c) periodic coexistence on the $x-w$ plane, (d) periodic coexistence on the $x-y-z$ space.

4. FPGA Implementation

Compared with analog circuits, digital circuits can better avoid environmental effects such as aging and temperature variations. Memristor-based chaotic systems are usually implemented in hardware using breadboards and amplifiers. Furthermore, hardware implementations of chaotic systems typically rely on integer-order chaotic systems.

This paper decides to implement the the system (19) by field-programmable gate array (FPGA). In this paper, a high-precision fourth-order Runge–Kutta (RK) method is used to discretized the Adomian resolving approach obtained in the above paper, as can be seen from the decomposition of the solution in Section 3.1. For the consideration of insufficient chip resources and other factors, after testing, this paper only realizes the solution of the first two items x_0 and x_1 . Finally, we chose Vivado as the experimental development tool because it can provide a floating-point IP core. The FPGA chip used is the XC7Z0202CLG400I, manufactured by Xilinx, while the development board is the AX7020pro, made by ALINX Company. For the floating-point standard, we have selected IEEE754 with a specific precision of 32 bits, comprising 1 bit for the sign, 8 bits for the exponent, and 23 bits for the mantissa.

Through numerical simulation and comparison, it is confirmed that the system meets the hardware implementation standards. In order to synthesize the code into logic gates and perform layout and routing using the synthesis tools provided by the FPGA vendor, we first construct a stable chaotic signal, and the clock module is set to output a stable clock signal so as to ensure that the original calculation module of the register module will be updated continuously with the iterative calculation results. The digital signal produced is subsequently transformed into an analog signal through a digital-to-analog converter (DAC) and relayed to an oscilloscope. Following these procedures, the Vivado simulation platform is utilized for synthesis and implementation. The bitstream file is generated and burned into the chip within the development board. The chaotic attractor phase diagram is generated successfully by connecting the development board to the oscilloscope. Using the control parameters in Figure 5, the simulation consequences are shown in Figure 11a,b, which are the phase diagrams on the $x-y$ and $x-z$ planes of the hyperchaotic attractor, and the corresponding Figure 11c,d show the oscilloscope results. Based on the experimental consequences, the hardware experimental consequences coincide with the MATLAB simulation consequences in Figures 5a and 11b. Table 1 lists the resource utilization required to implement the system project according to Vivado2018.3. It shows that implementing this chaotic system requires considerable resource overhead.

Table 1. Resource utilization efficiency in implementing chaotic system using FPGA.

Resource	Utilization	Available	Utilization
LUT	34212	53200	64.30
LUTRAM	1634	17400	9.39
FF	45313	106400	42.58
DSP	165	220	75
IO	34	125	27.20
BUFG	1	32	3.13

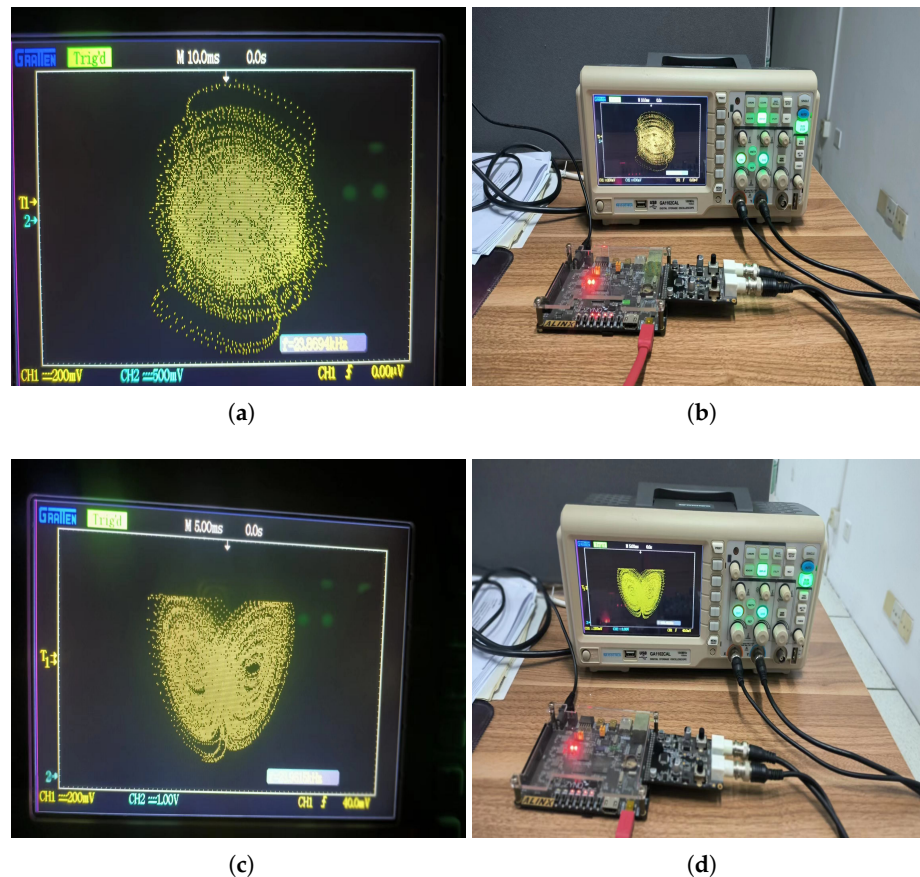


Figure 11. FPGA oscilloscope result diagrams and device diagrams. (a) Oscilloscope result diagram on the $x - y$ plane, (b) device diagram on the $x - y$ plane, (c) oscilloscope result diagram on the $x - z$ plane, (d) device diagram on the $x - z$ plane.

5. NIST Test

The technology of pseudo-random number generators is a fundamental technology in fields such as national defense security, privacy protection, encrypted communication, instrument and equipment manufacturing, and so on. PRNGs based on chaos have ergodicity and random behavior characteristics, which can avoid the shortcomings of a short period or correlation in general generators and have been widely used [16–20]. To utilize the proposed 5D FOMHS for pseudo-random generation, it is imperative to verify and assess the randomness and statistical properties of the purported randomness markers and actual randomness. Accordingly, this paper will conduct NIST testing using a statistical package comprising fifteen tests to quantify and evaluate the randomness of the digital sequence generated by an encrypted random or pseudo-random number generator. Following this, an analysis of chaotic sequences generated by fractional hyperchaotic systems will be provided. These sequences, spanning 100 million bits, are partitioned into $n = 100$ groups, each containing 1 million bits. The evaluation outcomes from NIST are summarized in

Table 2, indicating that the p -values of a total of fifteen statistical tests are greater than 0.01. Additionally, the formula for computing p -values $_T$ is as follows:

$$P - \text{values}_T = \text{igamc}\left(\frac{9}{2}, \frac{x}{2}\right), \quad (26)$$

where

$$x = \sum_{i=1}^{10} \frac{(F_i - (s/10)^2)}{s/10}, \quad (27)$$

where F_i represents the figure of p -values in the subinterval i , while s is the sample capacity. Evaluation criteria: The sequence is considered uniformly distributed when total p -values > 0.0001 .

Table 2. NIST test results.

No.	Statistical Test	p -Value	Proportion	p -Value $_T$
1	Frequency	0.051942	0.98	0.0645
2	Block Frequency	0.657933	0.99	0.7642
3	Cumulative Sums	0.534146	0.98	0.6577
4	Runs	0.275709	0.98	0.3781
5	Longest Run	0.534146	0.99	0.6577
6	Rank	0.383827	1	0.5055
7	FFT	0.759756	0.98	0.8406
8	Non-Overlapping Template	0.883171	1	0.9217
9	Overlapping Template	0.021999	0.99	0.0223
10	Universal	0.678686	0.98	0.7805
11	Approximate Entropy	0.262249	1	0.3611
12	Random Excursions	0.883171	1	0.0243
13	Random Excursions Variant	0.574903	1	0.0118
14	Serial	0.455937	1	0.5819
15	Linear Complexity	0.883171	0.98	0.9217

The histogram of non-overlapping templates provides a visual representation of the distribution and allows for a straightforward assessment of the sequence's uniformity. Histogram Figure 12 demonstrates that the allocation of the sequence is uniform. The consequences indicate that the fractional-order hyperchaotic model has passed all tests. Therefore, the proposed 5D FOMHS exhibits excellent random characteristics, meeting the application standards of pseudo-random generators.

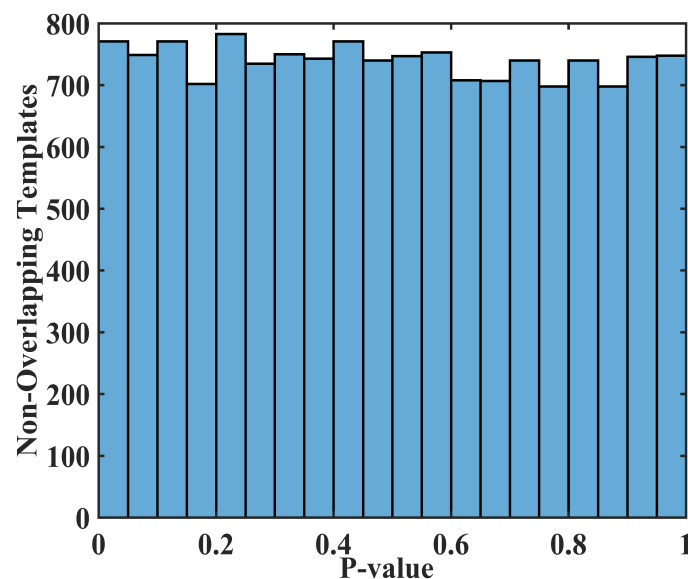


Figure 12. p -values histogram of non-overlapping templates.

6. Conclusions

This paper proposes a 5DFOMHS with multiple coexisting attractors by coupling a memristor to an integer-order system. Firstly, based on the definition of calculus, we use the Adomian decomposition method to decompose the terms in fractional-order differential equations for simulation and discretization purposes. In addition, we also used phase diagrams, time-domain diagrams, bifurcation diagrams, and Lyapunov exponent spectrum to study the dynamic motion characteristics of the system, discovering rich dynamic characteristics and application potential. Specifically, the system can generate multiple coexisting attractors with constant parameters. Subsequently, we implemented the first two items of 5D FOMHS on FPGA and obtained results consistent with the simulation phase diagram in Matlab. Finally, we evaluated 5D FOMHS using NIST tools, confirming its good randomness and potential for secure communication applications. Future work may explore applications in fields such as deep learning and biomedical research.

Author Contributions: Conceptualization, F.Y. and W.Z.; methodology, W.Z. and X.X.; software, W.Z. and W.Y.; validation, F.Y., W.Z. and S.C.; formal analysis, F.Y. and W.Z.; investigation, W.Z.; resources, F.Y. and S.C.; data curation, W.Z.; writing—original draft preparation, F.Y. and W.Z.; writing—review and editing, F.Y., W.Z. and C.W.; visualization, Y.L.; supervision, J.Z. and C.W.; project administration, F.Y. and W.Y.; funding acquisition, S.C. and J.Z. All authors have read and agreed to the published version of the manuscript.

Funding: This work was supported by the Natural Science Foundation of Hunan Province under Grants 2022JJ30624, 2022JJ10052, and 2021JJ30741; the Scientific Research Fund of Hunan Provincial Education Department under Grant 21B0345; the National Natural Science Foundation of China under Grant 62172058; and the Postgraduate Training Innovation Base Construction Project of Hunan Province under Grant 2020-172-48.

Institutional Review Board Statement: Not applicable.

Informed Consent Statement: Not applicable.

Data Availability Statement: The data that support the findings of this study are available from the corresponding author upon reasonable request.

Acknowledgments: The authors thank the editors and reviewers for their hard work, who have made outstanding contributions to the improvement of the quality of this article!

Conflicts of Interest: The authors declare no conflicts of interest.

References

1. Wang, X.; Zhao, M. A new spatiotemporal chaos model and its application in bit-level image encryption. *Multimed. Tools Appl.* **2024**, *83*, 10481–10502. [[CrossRef](#)]
2. Arab, A.; Rostami, M.J.; Ghavami, B. An image encryption method based on chaos system and AES algorithm. *J. Supercomput.* **2019**, *75*, 6663–6682. [[CrossRef](#)]
3. Wen, H.; Chen, R.; Yang, J.; Zheng, T.; Wu, J.; Lin, W.; Jian, H.; Lin, Y.; Ma, L.; Liu, Z.; et al. Security analysis of a color image encryption based on bit-level and chaotic map. *Multimed. Tools Appl.* **2024**, *83*, 4133–4149. [[CrossRef](#)]
4. Gao, X.; Mou, J.; Banerjee, S.; Zhang, Y. Color-Gray Multi-Image Hybrid Compression–Encryption Scheme Based on BP Neural Network and Knight Tour. *IEEE Trans. Cybern.* **2023**, *53*, 5037–5047. [[CrossRef](#)] [[PubMed](#)]
5. Liu, X.; Mou, J.; Zhang, Y.; Cao, Y. A New Hyperchaotic Map Based on Discrete Memristor and Meminductor: Dynamics Analysis, Encryption Application, and DSP Implementation. *IEEE Trans. Ind. Electron.* **2024**, *71*, 5094–5104. [[CrossRef](#)]
6. Xu, Q.; Wang, Y.; Chen, B.; Li, Z.; Wang, N. Firing pattern in a memristive Hodgkin–Huxley circuit: Numerical simulation and analog circuit validation. *Chaos Solitons Fractals* **2023**, *172*, 113627. [[CrossRef](#)]
7. Lai, Q.; Wan, Z.; Kuate, P.D.K. Generating grid multi-scroll attractors in memristive neural networks. *IEEE Trans. Circuits Syst. I Regul. Pap.* **2023**, *70*, 1324–1336. [[CrossRef](#)]
8. Kong, X.; Yu, F.; Yao, W.; Cai, S.; Zhang, J.; Lin, H. Memristor-induced hyperchaos, multiscroll and extreme multistability in fractional-order HNN: Image encryption and FPGA implementation. *Neural Netw.* **2024**, *171*, 85–103. [[CrossRef](#)]
9. Xu, Q.; Wang, Y.; Wu, H.; Chen, M.; Chen, B. Periodic and chaotic spiking behaviors in a simplified memristive Hodgkin–Huxley circuit. *Chaos Solitons Fractals* **2024**, *179*, 114458. [[CrossRef](#)]
10. Chen, M.; Wang, A.; Wu, H.; Chen, B.; Xu, Q. DC-Offset Strategy for Controlling Hidden and Multistable Behaviors in Physical Circuits. *IEEE Trans. Ind. Electron.* **2024**, *71*, 9417–9425. [[CrossRef](#)]

11. Yu, F.; Kong, X.; Yao, W.; Zhang, J.; Cai, S.; Lin, H.; Jin, J. Dynamics analysis, synchronization and FPGA implementation of multiscroll Hopfield neural networks with non-polynomial memristor. *Chaos Solitons Fractals* **2024**, *179*, 114440. [[CrossRef](#)]
12. Yao, W.; Wang, C.; Sun, Y.; Gong, S.; Lin, H. Event-triggered control for robust exponential synchronization of inertial memristive neural networks under parameter disturbance. *Neural Netw.* **2023**, *164*, 67–80. [[CrossRef](#)] [[PubMed](#)]
13. Xu, Q.; Liu, T.; Ding, S.; Bao, H.; Li, Z.; Chen, B. Extreme multistability and phase synchronization in a heterogeneous bi-neuron Rulkov network with memristive electromagnetic induction. *Cogn. Neurodyn.* **2023**, *17*, 755–766. [[CrossRef](#)] [[PubMed](#)]
14. Ma, M.; Xiong, K.; Li, Z.; He, S. Dynamical behavior of memristor-coupled heterogeneous discrete neural networks with synaptic crosstalk. *Chin. Phys. B* **2024**, *33*, 028706. [[CrossRef](#)]
15. Tan, F.; Zhou, L.; Lu, J.; Zhang, H. Fixed-time synchronization in multilayer networks with delay Cohen–Grossberg neural subnets via adaptive quantitative control. *Asian J. Control.* **2024**, *26*, 446–455. [[CrossRef](#)]
16. Zhu, S.; Deng, X.; Zhang, W.; Zhu, C. Construction of a new 2D hyperchaotic map with application in efficient pseudo-random number generator design and color image encryption. *Mathematics* **2023**, *11*, 3171. [[CrossRef](#)]
17. Abderrahim, N.; Benmansour, F.; Seddiki, O. FPGA Implementation of a Chaotic Pseudo-random Numbers Generator. *SN Comput. Sci.* **2023**, *4*, 410. [[CrossRef](#)]
18. Yang, Z.; Liu, Y.; Wu, Y.; Qi, Y.; Ren, F.; Li, S. A high speed pseudo-random bit generator driven by 2D-discrete hyperchaos. *Chaos Solitons Fractals* **2023**, *167*, 113039. [[CrossRef](#)]
19. Koubaâ, K.; Derbel, N. DNA Image Encryption Scheme Based on a Chaotic LSTM Pseudo-Random Number Generator. *Int. J. Bifurc. Chaos* **2023**, *33*, 2350067. [[CrossRef](#)]
20. Peng, H.; Ji'e, M.; Du, X.; Duan, S.; Wang, L. Design of pseudorandom number generator based on a controllable multi-double-scroll chaotic system. *Chaos Solitons Fractals* **2023**, *174*, 113803. [[CrossRef](#)]
21. Deng, Q.; Wang, C.; Lin, H. Memristive Hopfield neural network dynamics with heterogeneous activation functions and its application. *Chaos Solitons Fractals* **2024**, *178*, 114387. [[CrossRef](#)]
22. Wang, C.; Tang, D.; Lin, H.; Yu, F.; Sun, Y. High-dimensional memristive neural network and its application in commercial data encryption communication. *Expert Syst. Appl.* **2024**, *242*, 122513. [[CrossRef](#)]
23. Asif, S.; Zhao, M.; Li, Y.; Tang, F.; Zhu, Y. CGO-Ensemble: Chaos Game Optimization Algorithm-Based Fusion of Deep Neural Networks for Accurate Mpox Detection. *Neural Netw.* **2024**, *173*, 106183. [[CrossRef](#)] [[PubMed](#)]
24. Chai, X.; Tang, Z.; Gan, Z.; Lu, Y.; Wang, B.; Zhang, Y. SE-NDEND: A novel symmetric watermarking framework with neural network-based chaotic encryption for Internet of Medical Things. *Biomed. Signal Process. Control* **2024**, *90*, 105877. [[CrossRef](#)]
25. Lai, Q.; Wan, Z.; Zhang, H.; Chen, G. Design and Analysis of Multiscroll Memristive Hopfield Neural Network With Adjustable Memductance and Application to Image Encryption. *IEEE Trans. Neural Networks Learn. Syst.* **2023**, *34*, 7824–7837. [[CrossRef](#)] [[PubMed](#)]
26. Zhang, X.; Xu, J.; Moshayedi, A.J. Design and FPGA implementation of a hyperchaotic conservative circuit with initial offset-boosting and transient transition behavior based on memcapacitor. *Chaos Solitons Fractals* **2024**, *179*, 114460. [[CrossRef](#)]
27. Lai, Q.; Yang, L.; Chen, G. Design and Performance Analysis of Discrete Memristive Hyperchaotic Systems With Stuffed Cube Attractors and Ultraboosting Behaviors. *IEEE Trans. Ind. Electron.* **2024**, *71*, 7819–7828. [[CrossRef](#)]
28. Toktas, F.; Erkan, U.; Yetgin, Z. Cross-channel color image encryption through 2D hyperchaotic hybrid map of optimization test functions. *Expert Syst. Appl.* **2024**, *249*, 123583. [[CrossRef](#)]
29. Tang, D.; Wang, C.; Lin, H.; Yu, F. Dynamics analysis and hardware implementation of multi-scroll hyperchaotic hidden attractors based on locally active memristive hopfield neural network. *Nonlinear Dyn.* **2024**, *112*, 1511–1527. [[CrossRef](#)]
30. Feng, W.; Zhang, J.; Chen, Y.; Qin, Z.; Zhang, Y.; Ahmad, M.; Woźniak, M. Exploiting robust quadratic polynomial hyperchaotic map and pixel fusion strategy for efficient image encryption. *Expert Syst. Appl.* **2024**, *246*, 123190. [[CrossRef](#)]
31. Wei, Z.; Moroz, I.; Sprott, J.C.; Wang, Z.; Zhang, W. Detecting hidden chaotic regions and complex dynamics in the self-exciting homopolar disc dynamo. *Int. J. Bifurc. Chaos* **2017**, *27*, 1730008. [[CrossRef](#)]
32. Wei, Z.; Moroz, I.; Sprott, J.; Akgul, A.; Zhang, W. Hidden hyperchaos and electronic circuit application in a 5D self-exciting homopolar disc dynamo. *Chaos* **2017**, *27*, 033101. [[CrossRef](#)] [[PubMed](#)]
33. Wei, Z.; Zhang, W.; Yao, M. On the periodic orbit bifurcating from one single non-hyperbolic equilibrium in a chaotic jerk system. *Nonlinear Dyn.* **2015**, *82*, 1251–1258. [[CrossRef](#)]
34. Chen, C.; Min, F.; Cai, J.; Bao, H. Memristor Synapse-Driven Simplified Hopfield Neural Network: Hidden Dynamics, Attractor Control, and Circuit Implementation. *IEEE Trans. Circuits Syst. I Regul. Pap.* **2024**, 1–12. [[CrossRef](#)]
35. Dong, C.; Yang, M.; Jia, L.; Li, Z. Dynamics investigation and chaos-based application of a novel no-equilibrium system with coexisting hidden attractors. *Phys. A Stat. Mech. Its Appl.* **2024**, *633*, 129391. [[CrossRef](#)]
36. Tiwari, A.; Nathasarma, R.; Roy, B.K. A new time-reversible 3D chaotic system with coexisting dissipative and conservative behaviors and its active non-linear control. *J. Frankl. Inst.* **2024**, *361*, 106637. [[CrossRef](#)]
37. Al-Azzawi, S.F. Dynamical behavior of a new jerk system inspired from chaotic memory oscillators. *Arch. Control. Sci.* **2024**, *34*, 149–170. [[CrossRef](#)]
38. Fan, C.; Ding, Q. Dynamic analysis and geometric control of a novel parametrically controllable multi-scroll conservative chaotic system. *Nonlinear Dyn.* **2024**, *112*, 3935–3949. [[CrossRef](#)]
39. Kong, X.; Yu, F.; Yao, W.; Xu, C.; Zhang, J.; Cai, S.; Wang, C. A class of $2n+1$ dimensional simplest hamiltonian conservative chaotic systems and fast image encryption schemes. *Appl. Math. Model.* **2024**, *125*, 351–374. [[CrossRef](#)]

40. Yu, F.; Shen, H.; Yu, Q.; Kong, X.; Sharma, P.K.; Cai, S. Privacy Protection of Medical Data Based on Multi-Scroll Memristive Hopfield Neural Network. *IEEE Trans. Netw. Sci. Eng.* **2023**, *10*, 845–858. [[CrossRef](#)]
41. Lin, H.; Wang, C.; Sun, Y. A universal variable extension method for designing multiscroll/wing chaotic systems. *IEEE Trans. Ind. Electron.* **2024**, *71*, 7806–7818. [[CrossRef](#)]
42. Zhang, T.; Zhao, Y.; Xu, X.; Wu, S.; Gu, Y. Solution and dynamics analysis of fractal-fractional multi-scroll Chen chaotic system based on Adomian decomposition method. *Chaos Solitons Fractals* **2024**, *178*, 114268. [[CrossRef](#)]
43. Qin, M.; Lai, Q. Expanded multi-scroll attractor system analysis and application for remote sensing image encryption. *Appl. Math. Model.* **2024**, *125*, 125–146. [[CrossRef](#)]
44. Erkan, U.; Toktas, A.; Lai, Q. 2D hyperchaotic system based on Schaffer function for image encryption. *Expert Syst. Appl.* **2023**, *213*, 119076. [[CrossRef](#)]
45. Al-Azzawi, S.; Hasan, A.M. A New 4D Hidden Hyperchaotic System with Higher Largest Lyapunov exponent and its Synchronization. *Int. J. Math. Stat. Comput. Sci.* **2024**, *2*, 63–74. [[CrossRef](#)]
46. Huang, L.L.; Ma, Y.H.; Li, C. Characteristic analysis of 5D symmetric Hamiltonian conservative hyperchaotic system with hidden multiple stability. *Chin. Phys. B* **2024**, *33*, 010503. [[CrossRef](#)]
47. Yu, F.; Kong, X.; Chen, H.; Yu, Q.; Cai, S.; Huang, Y.; Du, S. A 6D fractional-order memristive Hopfield neural network and its application in image encryption. *Front. Phys.* **2022**, *10*, 847385. [[CrossRef](#)]
48. Sun, J.; Wang, Y.; Liu, P.; Wen, S.; Wang, Y. Memristor-based neural network circuit with multimode generalization and differentiation on pavlov associative memory. *IEEE Trans. Cybern.* **2022**, *53*, 3351–3362. [[CrossRef](#)] [[PubMed](#)]
49. Yu, F.; Kong, X.; Mokbel, A.A.M.; Yao, W.; Cai, S. Complex Dynamics, Hardware Implementation and Image Encryption Application of Multiscroll Memristive Hopfield Neural Network With a Novel Local Active Memristor. *IEEE Trans. Circuits Syst. II-Exp. Briefs* **2023**, *70*, 326–330. [[CrossRef](#)]
50. Yao, W.; Liu, J.; Sun, Y.; Zhang, J.; Yu, F.; Cui, L.; Lin, H. Dynamics analysis and image encryption application of Hopfield neural network with a novel multistable and highly tunable memristor. *Nonlinear Dyn.* **2023**, *112*, 693–708. [[CrossRef](#)]
51. Matouk, A.; Almutairi, D.; Herzallah, M.; Abdelkawy, M.; Abdelhameed, T. Symmetry in a Fractional-Order Multi-Scroll Chaotic System Using the Extended Caputo Operator. *Symmetry* **2023**, *15*, 1582. [[CrossRef](#)]
52. Lei, T.; Fu, H.; Zang, H.; Huang, L.; Sun, W. Adomian Decomposition, Firing Change Process Analysis and Synchronous Control of Fractional-Order Hindmarsh–Rose Neurons in Electromagnetic Field. *Processes* **2023**, *11*, 2568. [[CrossRef](#)]
53. Zeng, Y. A Laplace Adomian Decomposition Method for Fractional-Order Infection Model. *J. Appl. Math. Comput.* **2022**, *6*, 529–534. [[CrossRef](#)]
54. Wang, E.; Yan, S.; Sun, X.; Wang, Q. Analysis of bifurcation mechanism of new hyperchaotic system, circuit implementation, and synchronization. *Nonlinear Dyn.* **2023**, *111*, 3869–3885. [[CrossRef](#)]
55. He, S.; Sun, K.; Wang, H. Adomian decomposition method for fractional-order chaotic systems and its complexity analysis. *Acta Phys. Sin.* **2014**, *8*, 53360–53373.

Disclaimer/Publisher’s Note: The statements, opinions and data contained in all publications are solely those of the individual author(s) and contributor(s) and not of MDPI and/or the editor(s). MDPI and/or the editor(s) disclaim responsibility for any injury to people or property resulting from any ideas, methods, instructions or products referred to in the content.